Texture Development During Annealing in a Low-Carbon Formable Steel Containing Impurities from Increased Scrap Use

JIAQI DUAN, DIDIER FARRUGIA, CLAIRE DAVIS, and ZUSHU LI

Impurities (Cu, Sn, Cr, and Ni) have been added to a low-carbon formable strip steel to simulate the scenario of increased use of scrap during steel production. Texture evolution during annealing of the cold-rolled base steel and impurity-added steel have been investigated. The impurities were shown to suppress the development of the γ-fiber texture. Meanwhile, a higher fraction of random orientations was developed in the impurity-added steel. However, the adverse effect of impurities on the γ-fiber was mitigated during annealing at higher temperatures (650 °C to 750 °C). The correlation between texture development and microstructure heterogeneity, and the effect of impurity additions on texture development are discussed. This work provides guidelines on recycling scrap for the production of low-carbon formable steels.

I. INTRODUCTION

STEEL is the most recycled material in the world. Recycling steel scrap for steel production *via* the Electric Arc Furnace (EAF) route or Blast Furnace–Basic Oxygen Steelmaking (BF-BOS) route can significantly reduce CO_2 emissions, and helps drastically reduce steels carbon footprint.[1] EAF routes can use 100 pct steel scrap, or a mixture of scrap and direct reduced iron, while the blast furnace–basic oxygen furnace steelmaking (BF-BOF) route can use up to 25 pct scrap steel.[2] However, the steel scrap often contains impurities that cannot be removed by the steelmaking process, such as Cu and Sn. The impurity content depends on the quality of the scrap and the amount of scrap used as feedstock in steelmaking;[3] and the impurity content will accumulate in final steel products with an increase in recycling cycles. The effect of impurities has been investigated in a hot-rolled low-carbon steel with regard to microstructure, but also effect of residuals on transformation kinetics and grain size, and hence mechanical properties.[4]

Low-carbon formable steels are primarily used for drawing applications. Good drawability requires a high degree of true strain in the planar direction and good resistance to plastic flow in the thickness direction; meanwhile the planar anisotropy should be low to reduce the extent of earing. Since drawability is strongly influenced by the crystallographic orientations, studies of the development of deformation and annealing textures are of great importance for the formability of low-carbon and ultra-low-carbon steels.[5–11]

It is well known that two types of fiber textures are developed during cold rolling of ferritic steels, partial α-fiber with ⟨110⟩//rolling direction (RD), and γ-fiber with {111}//normal direction (ND).[12,13] The partial α-fiber starts at {001} ⟨110⟩ and ends at {111} ⟨110⟩, which also belongs to the γ-fiber. Conventional models, such as 'relaxed constraints'[14] and 'self-consistent'[15] models, can be used to predict the cold rolling textures. Advanced models[16] have been developed to achieve more precise predictions in terms of the texture intensities. It has been confirmed that the deformation is heterogenous when reduction is < ~ 80 pct, with grains with a γ-fiber orientation undergoing a higher degree of deformation than α-fiber orientation grains, *i.e.,* the grain microstructure and stored energy are strongly correlated with the orientation of the grains.[17–20] The γ-fiber grains exhibit a higher density of geometrically necessary dislocations (GND), *i.e.,* higher orientation gradients and more low-angle boundaries (LABs), hence higher stored energy compared to α-fiber grains.[21,22] This affects the recovery and recrystallization processes during annealing after cold rolling, for example, the γ-fiber grains show a quicker formation of new grains than α-fiber grains as the higher stored energy provides a

JIAQI DUAN, CLAIRE DAVIS, and ZUSHU LI are with the Warwick Manufacturing Group, The University of Warwick, Coventry, CV4 7AL, UK. Contact e-mail: Jiaqi.Duan@warwick.ac.uk DIDIER FARRUGIA is with the Tata Steel R&D (UK), Material Design and Characterization, Coventry, CV4 7EZ, UK.

higher driving force for nucleation (recovery).[23–25] Kapoor *et al.*[26] observed faster recovery in γ-fiber grains than in α-fiber grains during a quasi *in-situ* annealing experiment on a cold-rolled low-carbon steel. As annealing proceeds, the newly formed grains enjoy a growth advantage and consume surrounding unrecrystallized regions.[27] Meanwhile, selective growth mechanism was proposed to account for the texture evolution.[28] In this theory, the ⟨110⟩ 26.5 deg boundaries exhibit higher mobility, accordingly, grains of {111} < 112 > orientations will grow faster than other grains when they are surrounded by deformation structure of {112} ⟨110⟩ orientations.

Texture evolution is known to be affected by the presence of alloying elements.[6] It has been proposed that interstitial atoms, *e.g.*, C and N, can interact with substitutional atoms, *e.g.*, Mn, forming complexes that can pin dislocations at elevated temperatures, thus adversely affecting the formation of new γ-fiber grains.[29] The addition of Ti and Nb can enhance the development of γ-fiber by fixing the C and N in precipitates.[30] Although there is abundant literature on the mechanisms through which the microstructure and textures develop in the rolled and annealed steels, there is no information on how impurities, at the level relevant to that likely to arise in low-carbon formable steels from increased scrap use, affect the microstructure and texture evolution during annealing, which is crucial for the formability of the steel. In this work, impurities (Cu, Cr, Ni, and Sn) have been added to a formable low-carbon steel to mimic the scenario of scrap utilization in steel production. Comparisons in annealing microstructure and textures have been made between the steels with and without impurity additions.

II. EXPERIMENTAL PROCEDURE

The chemical compositions of the steels under investigation are shown in Table I. The 'Base' steel represents the composition of the low-carbon formable steel produced *via* the BF-BOF steelmaking route. The 'Residual Scrap (RS)' steel, with impurity elements Cu, Ni, Cr, and Sn, represents the simulated composition when scraps containing high levels of impurities are used for production. The only difference in composition between the Base and RS steel is that the later contains impurity elements, *i.e.*, Cu, Ni, Cr, and Sn. Therefore, the influence of other elements on texture evolution can be ruled out. Ingots of 25 kg were cast using a vacuum induction melter in Tata Steel IJmuiden. Ingots of 100 mm thick were heat treated at 1220 °C for 60 minutes, hot rolled to 32 mm transfer bars in six passes. Then, the transfer bars were heated to above 1100 °C and finish rolled to 3 mm sheets in six passes with a finish rolling temperature of ~ 900 °C (above the recrystallization stop temperature (TNR)[31]). After hot rolling and phase transformation during cooling, textures were expected to be weak in both steels. Meanwhile, their

grain sizes were comparable. The average grain sizes measured from the mid-thickness position are 16 and 13 μm for the Base and RS steel, respectively. Thus, any difference observed in texture evolution between the Base and RS steel were not originated from hot rolling.[6] Subsequently, the sheets were cold rolled to 0.8 mm, giving around 73 pct cold-rolled reduction. The principal directions of the sheets are denoted as the rolling direction (RD), transverse direction (TD), and normal direction (ND). Cold-rolled samples were put into the pre-heated muffle furnace for static annealing at 550 °C to 750 °C, for up to one hour. After the annealing experiments, samples were removed from the furnace and cooled in air.

Electron backscattered diffraction (EBSD) scans were performed using an Oxford EBSD system attached to a JEOL SEM to reveal the microstructural features and orientation information in both the Base and RS steels after cold rolling and annealing, with step sizes varying from 0.075 to 1 μm, depending on the feature size. The scans were carried out from the quarter thickness to the center thickness to exclude any surface effects such as frictional shear deformation on rolling. EBSD samples were prepared by mechanical polishing, using 0.05 μm colloidal silica for the final polishing stage. The microstructure and crystallographic information were determined by using AZtecCrystal software. Quantification of the texture components was determined using the area fraction that belongs within 15 deg spread of that component. In addition to α- and γ-fiber, {411} ⟨148⟩ was also considered. After excluding the two fibers, {411} ⟨148⟩ became the dominant texture component while other components were insignificant in the orientation distribution function (ODF) maps of the deformed steels. The {111} ⟨110⟩ component at the intersection of the α- and γ-fiber was assigned to the γ-fiber. Orientations excluded from α-fiber, γ-fiber and {411} ⟨148⟩ were considered as random orientations. The crystallographic boundaries were classified based on their misorientations, *i.e.,* > 15 deg misorientations for high-angle boundaries (HABs, denoted in black in EBSD maps), and 2 to 15 deg misorientations for low-angle boundaries (LABs, denoted in gray in EBSD maps). Transmission Electron Microscopy (TEM) observation was carried out using a FEI TALOS operated at 200 kV. TEM specimens were prepared using focused ion beam (FIB) lift-out using a Versa Dualbeam.

III. RESULTS

A. *Cold-Rolled Microstructure and Texture*

Figures 1(a) and (b) show the overall microstructures in the RD–ND cross-section in the cold-rolled Base and Residual Scrap (RS) steels, respectively. For both steels, the microstructures are characterized by thin lamellar bands (LB) elongated along the RD, which are characteristic features in high strain rolled microstructures.[32]

Table I. Chemical Compositions of the Base and the Residual Scrap (RS) Steels (Wt Pct)

	C	Mn	Al + S + B	Cr	Ni	Cu	Sn
Base	0.024	0.165	0.036	—	—	—	—
RS	0.021	0.162	0.037	0.122	0.163	0.153	0.041
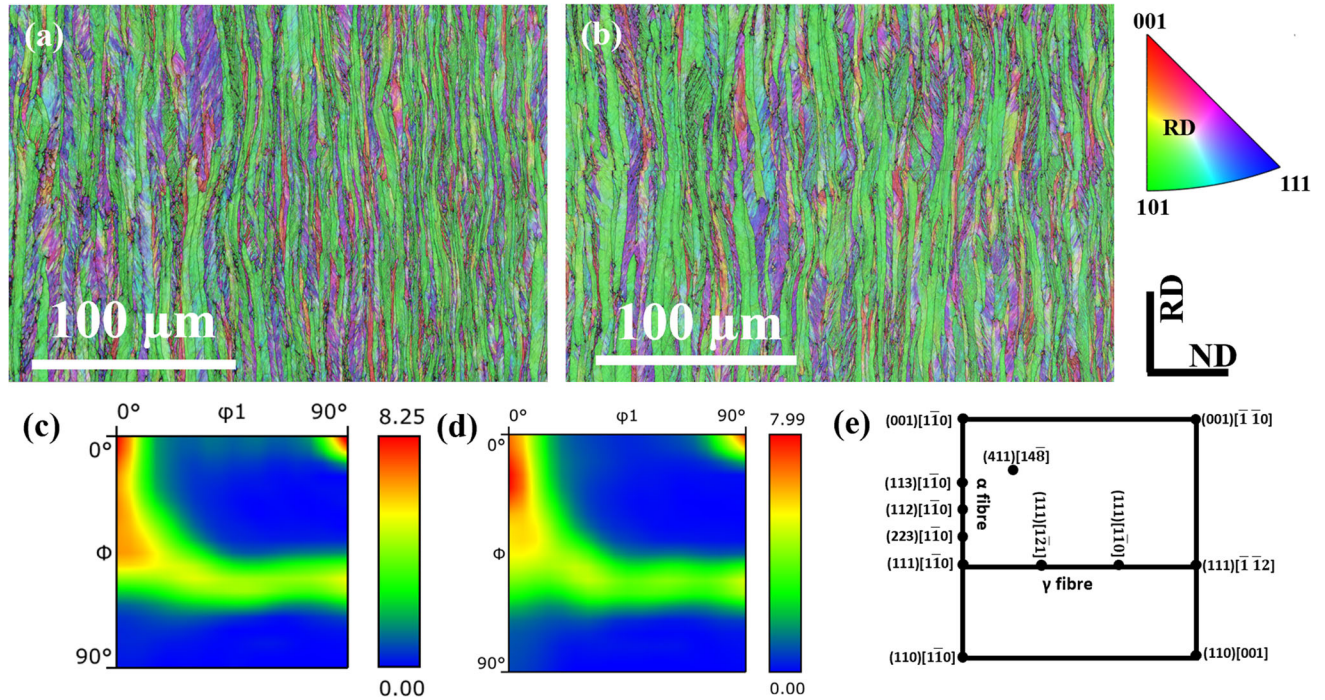
Fig. 1—EBSD maps showing the lamellar grains after cold rolling in the (*a*) Base and (*b*) Residual Scrap (RS) steels, and the $\phi_2 = 45$ deg section of orientation function (ODF) for the (*c*) Base and (*d*) RS steels. (*e*) gives the location of important texture components at $\phi_2 = 45$ deg section of ODF.

LBs are divided by HABs, and the average thickness of these bands in the Base and RS steel is 3.7 and 3.5 μm, respectively. The addition of impurities did not cause any visible difference in the cold-rolled microstructure.

The crystallographic textures for the cold-rolled Base and RS steels are presented in the $\phi_2 = 45$ deg section of ODF in Figures 1(c) and (d), respectively. For both steels, the orientations comprise the typical α-fiber and γ-fiber. The area fractions of α-fiber in the Base and RS steel are 0.394 and 0.411, respectively; and those of γ-fiber in the Base and RS steel are 0.402 and 0.387, respectively. In addition, the {411} ⟨148⟩ texture component was also developed, and its fraction was measured at 0.101 in the Base steel and 0.110 in the RS steel. The {411} ⟨148⟩ component belongs to the {h11} < 1/h 1 2 > R-fiber, which is parallel to the α fiber in the $\varphi_2 = 45$ deg section of the ODF. It has been proposed that this component forms when the α-fiber is highly deformed, and shearing is involved to maintain strain compatibility. When deformation deviates from pure plane strain conditions, the α-fiber rotates toward the {411} ⟨148⟩ component.[22,33] Overall, the cold-rolled Base and RS steels appear to exhibit similar textures (See Figure 1).

B. Heterogeneity in Deformed Microstructure

Deformation generates geometrically necessary dislocations (GNDs) that lead to the formation of orientation gradients in the form of intragranular misorientations and LABs. Further deformation could promote some rotation of the subgrains, and the former LABs becomes HABs. Figure 2 gives a high-magnification EBSD image of the cold-rolled Base steel for a closer examination of the deformation microstructure. The microstructure is not homogenous as some regions appear to exhibit higher local misorientations and finer structures than other regions, implying heterogeneities in deformation. Various regions were chosen to illustrate the different deformation microstructures, and their corresponding orientations are displayed in the {200} pole figures.

Region 1 appears smooth without any sharp features. The orientations of this region are close to {100} < 011 > from α-fiber, and they are highly concentrated. In Region 2, the area is divided by LABs and show some orientation spreading, *i.e.,* ~ 6 deg in the pole figure. This region is oriented near {311} < 011 >, *i.e.*, part of the α-fiber. It appears that Region 2 was subjected to a higher deformation than Region 1.
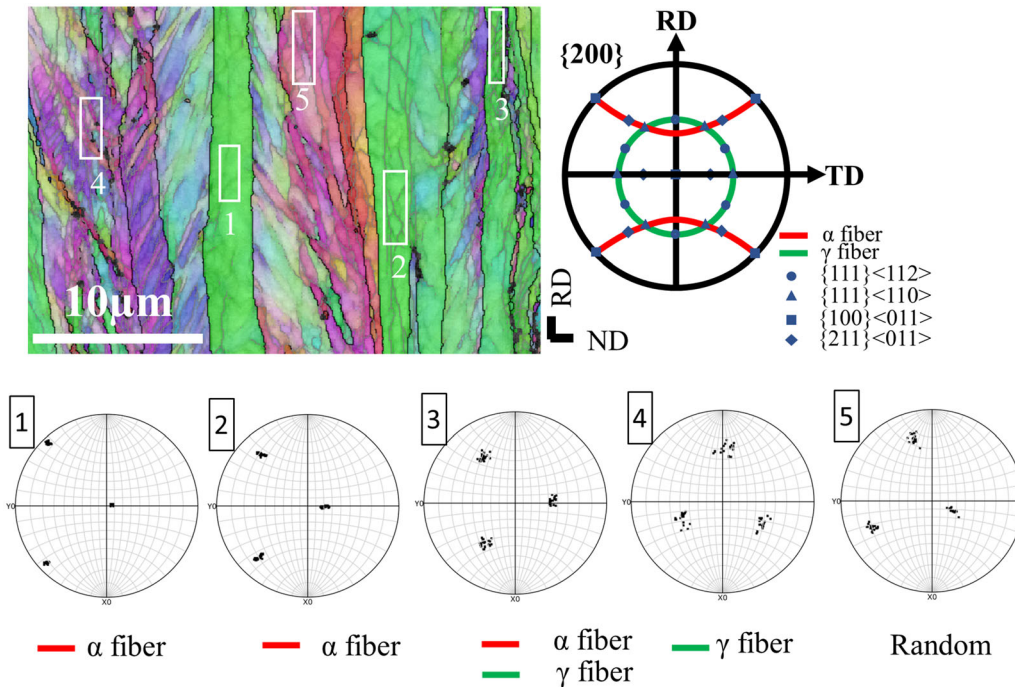
Fig. 2—EBSD orientation map of the cold-rolled Base steel showing a heterogeneous deformation microstructure. Region 1 (γ-fiber), Region 3 (random orientations), and Region 5 (from the intersection of α-and γ-fiber) show relatively fine substructures and a large spread of orientations; Region 4 (α-fiber) shows coarse substructures and a mild orientation spread; Region 2 (α-fiber) shows no substructure and exhibits clustered orientations. Locations of the important texture components are given at {200} pole figure.

Regions 3 and 4 exhibit similar microstructures. In contrast to Region 1, they show large orientation spreads, *e.g.*, ~ 15 deg, and refined subgrains. The orientations of Regions 3 and 4 are centered near {111} ⟨110⟩ and {111} < 112 > , *i.e.,* part of the γ-fiber, respectively. Region 5, an area with a random orientation, exhibits microstructural characters similar to those in Regions 3 and 4. The results suggest that Regions 3–5 underwent a higher degree of deformation than Regions 1–2.

Kernel average misorientation (KAM) was calculated to reveal the correlation between the local misorientations with the orientations in the deformed structures. The KAM value of a pixel from the EBSD map was calculated by averaging the misorientations between this pixel and every other pixel around the perimeter, and the KAM was calculated for each pixel of the map. The Kernel size was set as 5×5. Misorientations over 5 deg were discarded to exclude distinct subgrain and grain boundaries. Structures along α-fiber and γ-fiber orientations were divided into subgroups with a step size of 10 deg, and the average KAM values were obtained for each subgroup. Figure 3 shows the average KAM value of each subgroup along the α-fiber and γ-fiber in both the Base and RS steels. The results indicate that, in both steels, the misorientations are low in α-fiber grains of low Φ, but they increase with the increasing Φ. In comparison, γ-fiber grains exhibit higher misorientations, except at the intersection of the α- and γ-fiber. In addition, the results do not show significant variations in the KAM values along the γ-fiber. The average KAM

values for the {411} ⟨148⟩ and random orientations in both steels are also marked in Figure 3 for reference.

Moreover, grain boundary (GB) areal densities were calculated in the deformed structures of the different textures. Briefly, the deformed microstructures were divided into subsets in the EBSD map based on their orientations, *i.e.*, α-fiber, γ-fiber, {411} ⟨148⟩ and random orientations. Each subset was dilated by one pixel, and the length of the GBs in each subset was measured. The areal density of the GBs in each subset was obtained *via* dividing the GBs length by the area of the subset. Note that the GB between two adjacent subsets were counted in both subsets. Figure 4 shows the areal density of three types of GBs, *i.e.*, 2–5 deg LAB, 5–15 deg LAB, and > 15 deg HAB, in the regions of different orientations. The results reveal that the distributions of GBs are orientation dependent in the deformed structures in both Base and RS steels. For every GB type, the α-fiber shows the lowest GB density. The γ-fiber and random orientations contain comparable LAB density (2–5 deg & 5–15 deg). The highest HAB density (> 15 deg) is found in the random orientation regions.

C. *Annealing Microstructure*

Figure 5 shows EBSD maps of the Base and RS steels with annealing times for 1, 10, and 60 minutes at 550 °C. After 1 minute, new grains appeared in the deformed structure in the Base steel, as marked by arrows in Figure 5(a1). In contrast, the RS steel retained
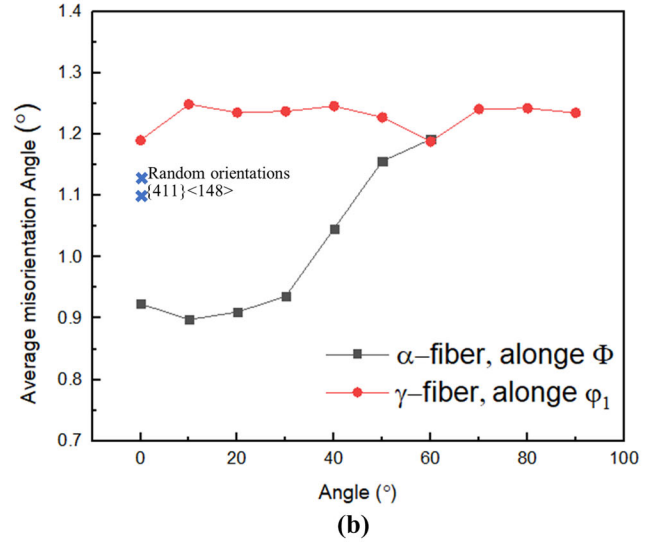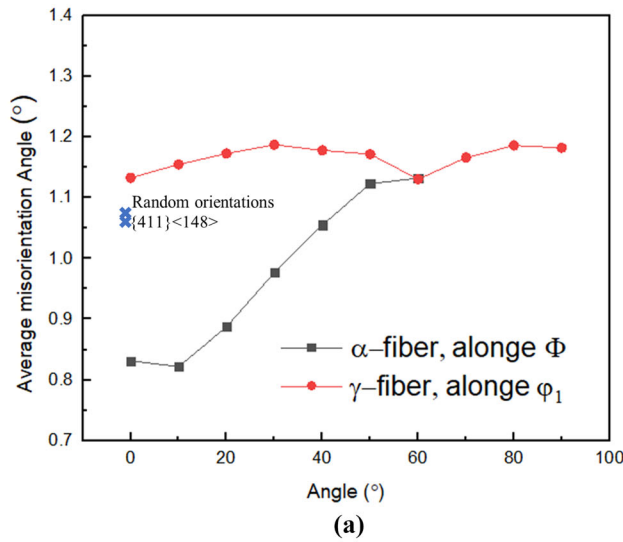
Fig. 3—Kernel average misorientation (KAM) along α-and γ-fiber in the cold rolled: (*a*) Base and (*b*) Residual Scrap (RS) steel. The KAM values of the {411} ⟨148⟩ and random orientations are marked in the plot.
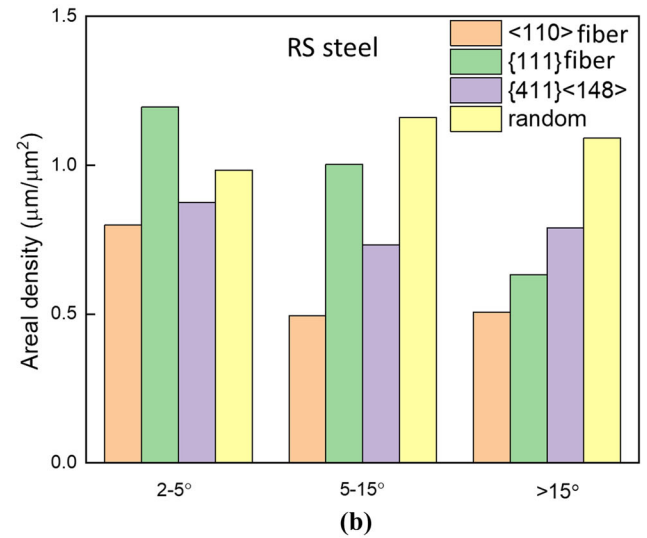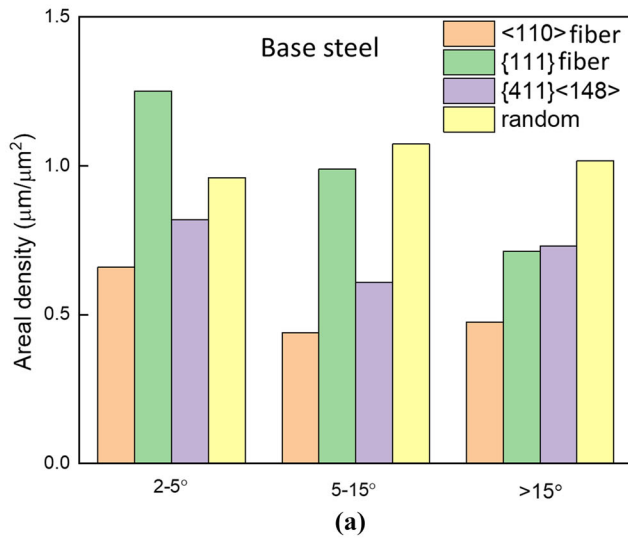

Fig. 4—Areal density of 2–5 deg LAB, 5–15 deg LAB, and > 15 deg HAB in the regions of various orientations in (*a*) Base and (*b*) Residual Scrap (RS) steel.

the deformation structures without any change observed. Note that the majority of the new grains are found in the vicinity of the boundaries of the deformed lamellar grains. After 10 minutes, the Base steel was partially recrystallized, while some new grains were sparsely observed in the RS steel. After 60 minutes, the Base steel showed full recrystallization, while some unrecrystallized bands could still be observed in the RS steel. Increasing the annealing temperature to 600 °C caused more rapid recrystallization in both steels, as shown in Figure 6. After 1 minute, about 90 pct of the structure was recrystallized in the Base steel; and the formation of the new grains was evident in the RS steel. Both steels reached complete recrystallization after 10 minutes of annealing at 600 °C. At 650 °C and

above, recrystallization finished within 1 minute (Figure 6) in both steels, followed by grain growth during the subsequent annealing. The grain size changes in both steels during grain growth were measured from the EBSD maps (GB threshold: 15 deg), and the results are given in Figure 7. The results show that grain growth was less in the RS steel.

Figure 8 compares the hardness changes between the Base and RS steels during isothermal annealing at various temperatures. At 550 °C, the Base steel showed a large drop in hardness in the first 10 minutes due to recrystallization, followed by a minor decrease during the subsequent annealing time. In contrast, the RS steel showed a slight decrease in hardness in the first 10 minutes, followed by continuous softening. By the
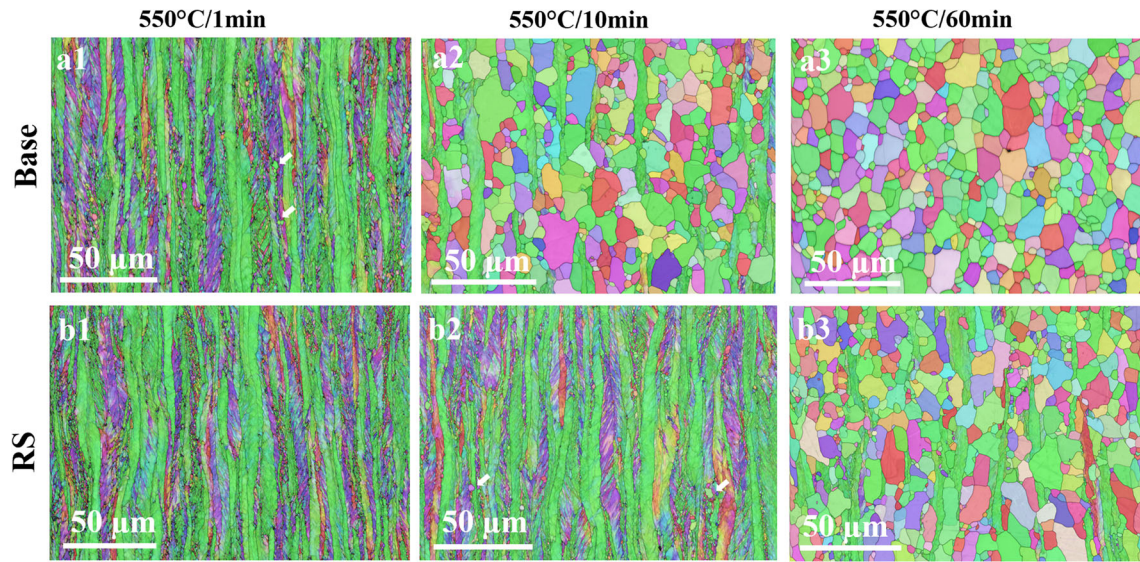
Fig. 5—EBSD maps of the (*a1-3*) Base and (*b1-3*) Residual Scrap (RS) steel subjected to annealing at 550 °C for various time. The Base steel showed a faster recrystallization kinetics than the RS steel. Example of new grain formation near the BGs are marked by arrow in (*a1*) and (*b2*).
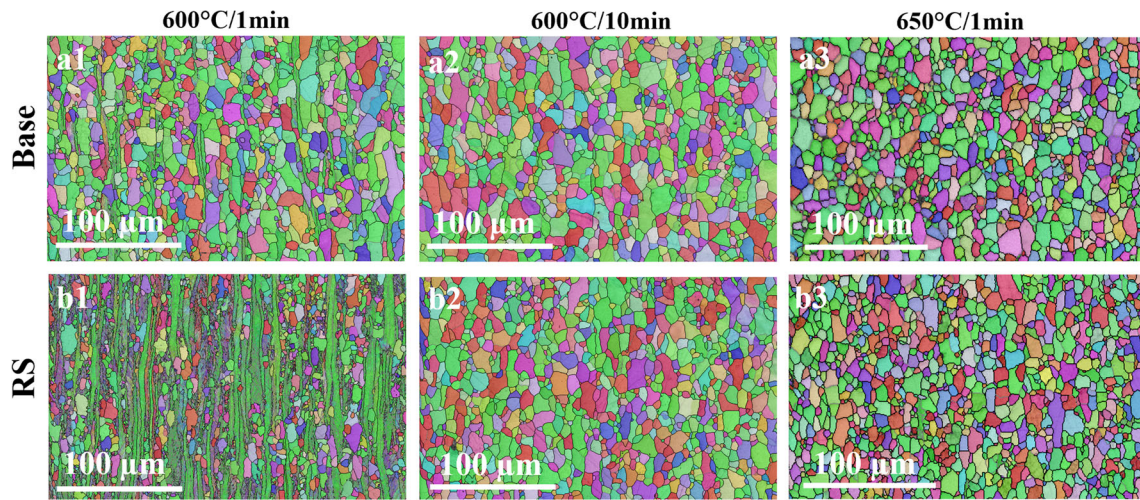

Fig. 6—EBSD maps of the (*a1-3*) Base and (*b1-3*) Residual Scrap (RS) steel subjected to annealing at 600 °C and 650 °C. Both steels completed the recrystallization within 10 min at 600 °C and within 1 min at 650 °C.
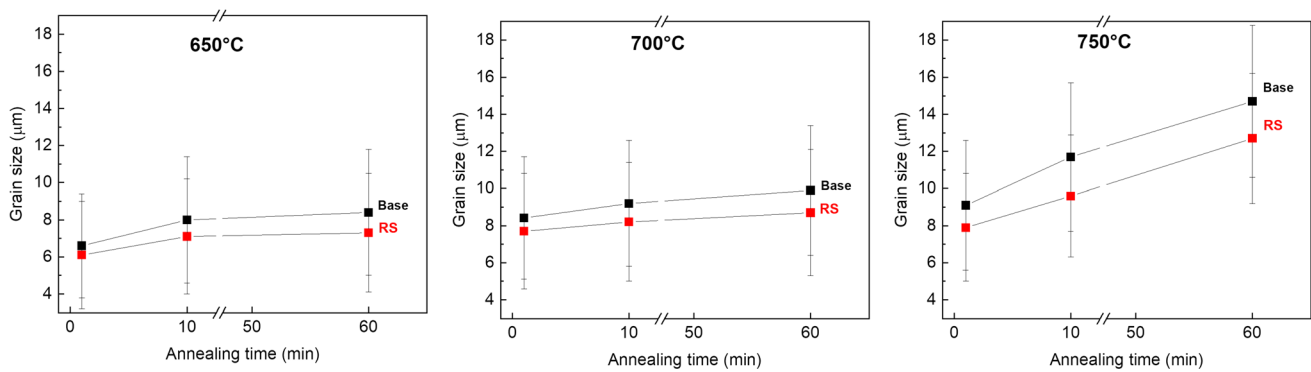

Fig. 7—Grain size changes after annealing at various temperatures and time in the Base and Residual Scrap (RS) steel.
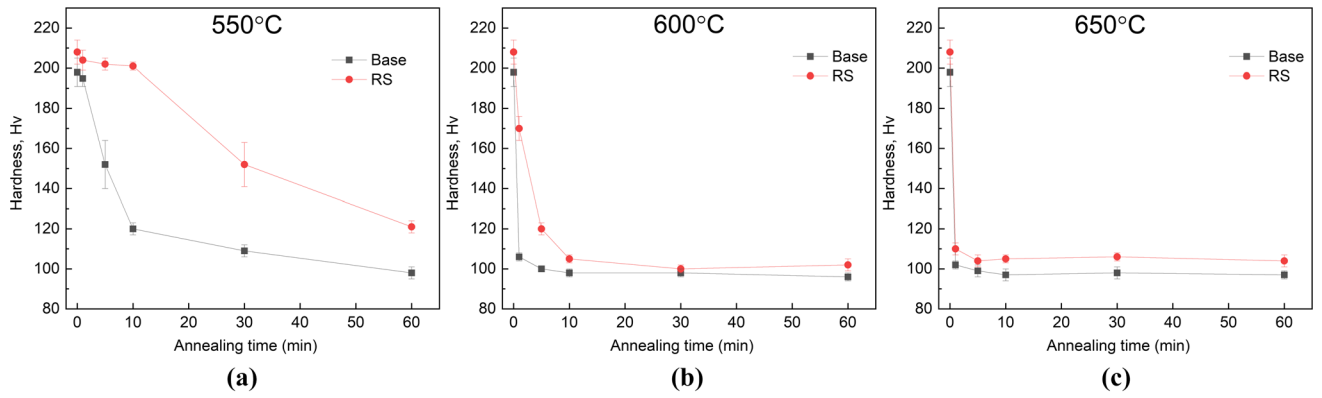
Fig. 8—Vickers's hardness changes in the cold-rolled Base and Residual Scrap (RS) steel after annealing at (a) 550 °C, (b) 600 °C, and (c) 650 °C for up to 60 min.
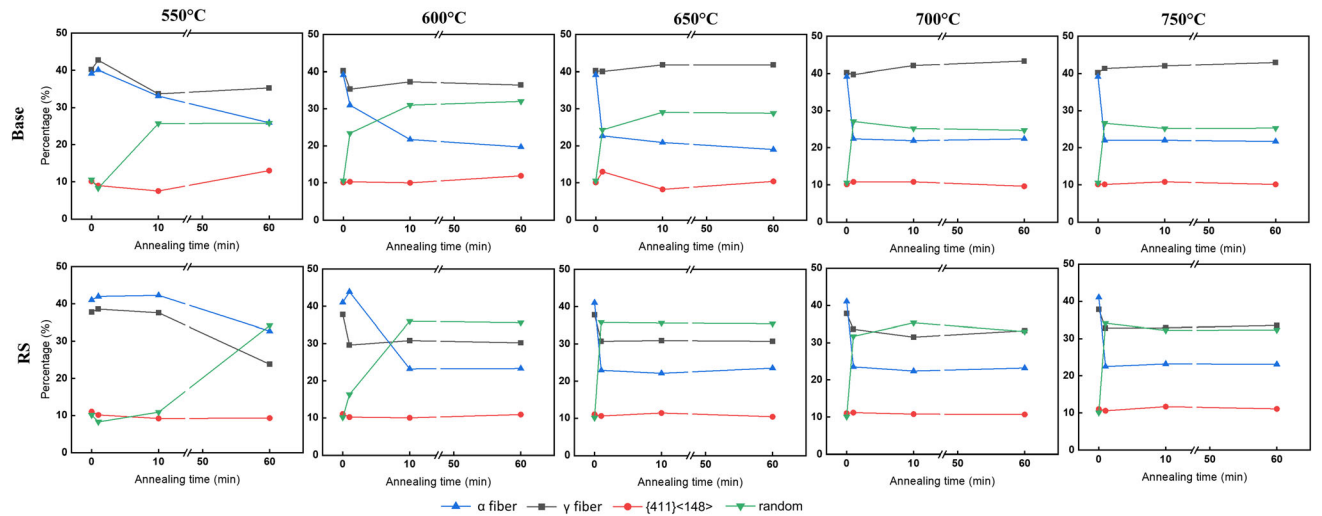

Fig. 9—Evolution of the fractions of the various orientations during annealing at various temperature and time in the Base and Residual Scrap (RS) steel.

end of the annealing, the RS steel still exhibited a noticeably higher hardness than the Base steel. Increasing annealing temperature to 600 °C caused more rapid decrease in hardness in both steels. The hardness in the Base steel dropped significantly in the first minute and slowly decreased until 10 minutes, before it became stable during the following annealing time. The hardness changes in the RS steel resembled the pattern in the Base steel, but the changes were more sluggish. The hardness results agree with the microstructure observations that Base steel exhibited a faster recrystallization kinetics than RS steel. At 650 °C and above (not shown), the hardness in both steels dropped significantly in the first minute and became stable thereafter.

D. *Annealing Texture*

The fraction changes of the main texture components and random orientations in the Base and RS steels during annealing are given in Figure 9. The key observations when comparing the behavior of the two steels are summarized as follows:

Similarities

- The changes in the fractions of textures mainly occurred during recrystallization, while during the grain growth stage the textures remained relatively stable. For example, at higher temperatures, major changes in textures only took place in the first minute when recrystallization happened.
- Significant weakening was found in the α-fiber at all annealing temperatures. For example, in the Base steel, the α-fiber fraction was reduced from 0.392 in the deformed condition to 0.221 after recrystallization at 750 °C.
- During recrystallization, random orientations increased their fractions. The {411} ⟨148⟩ component showed negligible variations.

Differences

- During recrystallization, the γ-fiber fraction decreased at lower annealing temperatures (550 °C to 600 °C) and remained stable at higher annealing temperatures (650 °C to 750 °C) in the Base steel.

Whereas in the RS steel, the γ-fiber fraction decreased at all temperatures, and greater decreases are found at lower temperatures.

- In each annealing condition, a higher fraction of γ-fiber and a lower fraction of α-fiber are found in the Base steel. Fraction ratios of γ/α fiber in the Base and RS steels after cold rolling and annealing at various temperatures for 60 minutes are given in Figure 10. The Base steel always displays a higher γ/α ratio than the RS steel.
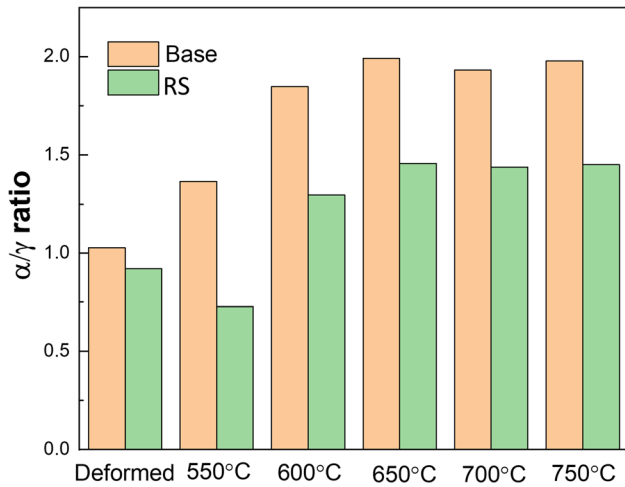

Fig. 10—Fraction ratios of γ/α-fiber in the Base and Residual Scrap (RS) steel after annealing at various temperatures for 60 min.

- In each annealing condition, a higher fraction of random orientations is found in the RS steel than in the Base steel. After the RS steel was recrystallized at lower temperatures (< 650 °C), the random orientations occupied a higher fraction than the γ-fiber; as the temperature increased, their fractions became comparable. By comparison, the fraction of random orientations was always lower than that of γ-fiber in the recrystallized Base steel.

The textures of the Base and RS steels after annealing at certain temperatures are presented in $\phi_2 = 45$ deg section of ODF in Figure 11. After 550 °C/60 minutes annealing, the Base steel still showed evidence of α-fiber and γ-fiber in the ODF, but the α-fiber appeared weakened. Whereas in the RS steel, the textures consisted of an incomplete γ-fiber and an α-fiber with a maximum at {100} ⟨110⟩. At 650 °C and 750 °C, both steels saw the weakening of the α-fiber and strengthening of the γ-fiber in the ODF. At 750 °C, the maximum intensity was found around the {111} ⟨110⟩ component. Note that the weakening of the α-fiber is not homogenous. Figure 12 gives the normalized density profiles along α-fiber in the deformed and 750 °C/60 minutes Base steel. The decrease in intensity is more significant at lower Φ, e.g., the {100} ⟨110⟩ at Φ = 0 deg component was subjected to the greatest weakening.

To capture the early stage in the formation of the recrystallization textures, the newly recrystallized grains were separated from the deformed microstructures in the 550 °C/1 minute Base steel and 550 °C/10 minutes
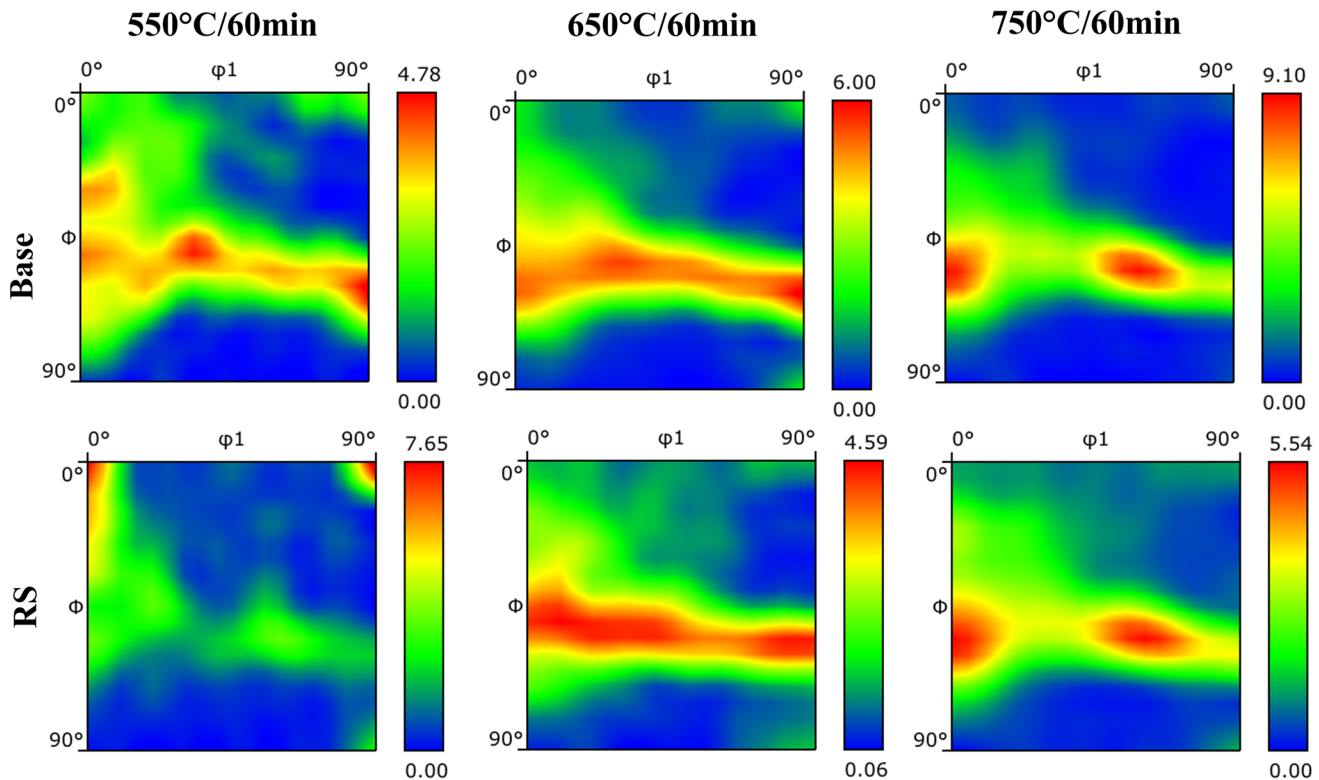

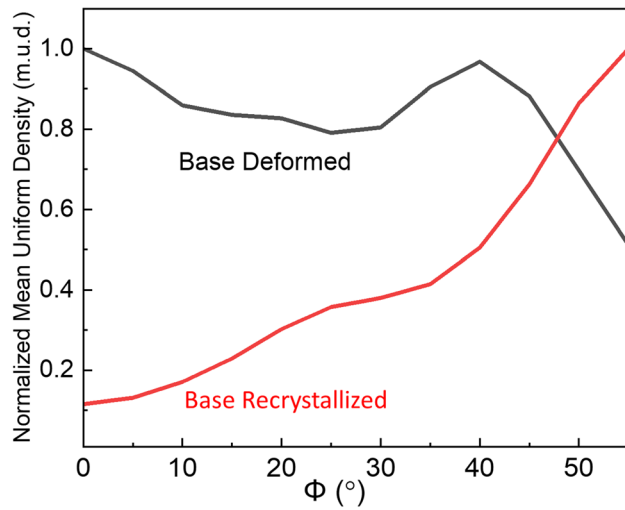Fig. 11—$\phi_2 = 45$ deg section of ODF showing the textures in both steels in various annealing conditions.

Fig. 12—The normalized density profile along α-fiber as a function of Φ (when $\phi_2 = 45$ deg and $\phi_1 = 0$ deg) for the Base steel in the deformed condition and the recrystallized (750 °C/60 min annealed) condition, respectively.

RS steel, respectively, Figure 13. The corresponding $\phi_2 = 45$ deg section of ODFs for the new grains are also given in Figure 13. Here, new grains were defined as regions: a. surrounded by HABs; b. minimum equivalent circle diameters of 1 μm; c. fitted ellipse aspect ratio is less than 3; and d. mean orientation spread is less than 3 deg. Manual inspection of the selection of the new grains indicated that the criteria chosen here are reasonable. Note that these new grains are not necessarily 'recrystallization nucleus' because they probably already underwent some degree of growth. The ODFs show that in both steels, γ-fiber was developed while α-fiber was weakened in the new grains, with significant intensity decrease of the {100} ⟨110⟩ component. Meanwhile, it appears that the γ-fiber was stronger in the new grains from Base steel. By comparing the ODF in Figure 13(c) to that of the 550 °C/60 minutes fully recrystallized Base steel in Figure 11, it is concluded that the textures developed in the early stage of recrystallization resembled the overall textures after recrystallization.
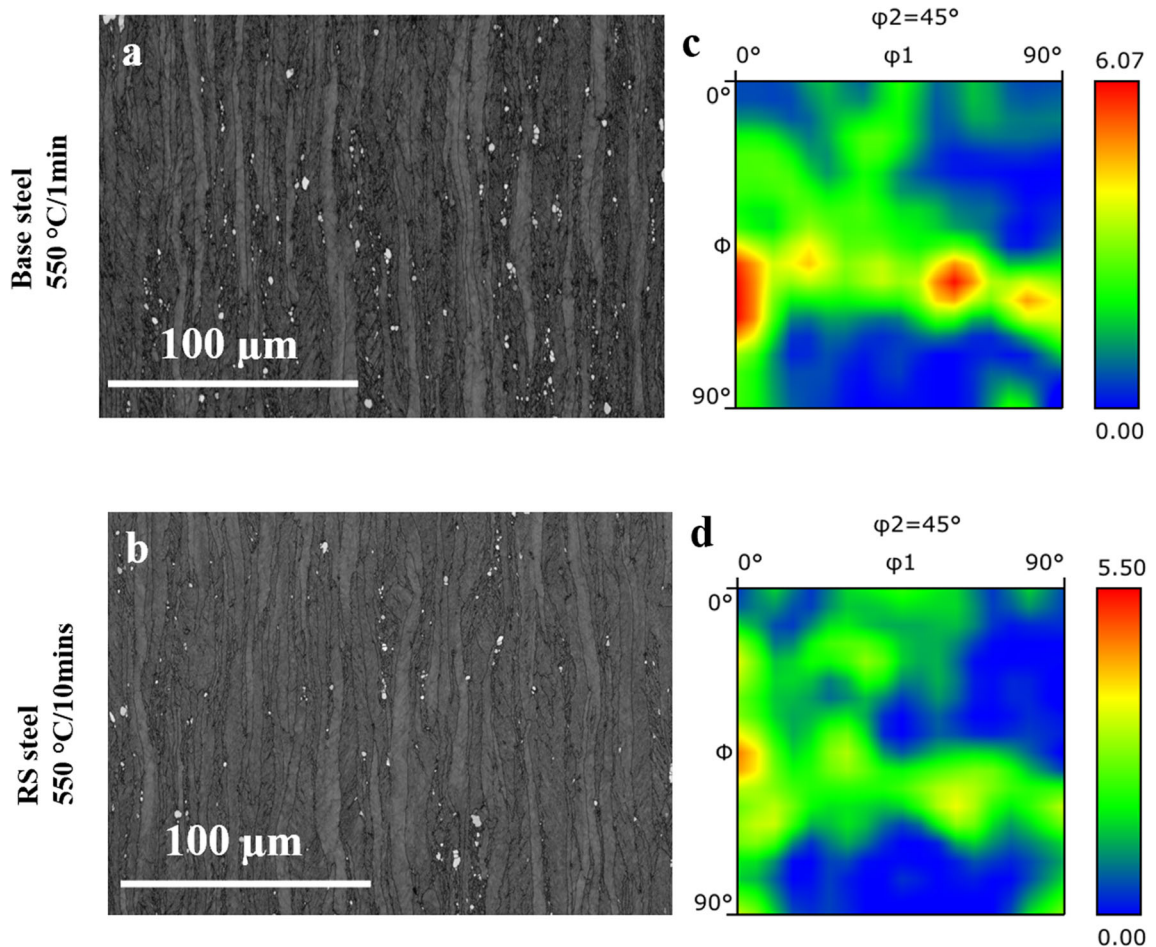

Fig. 13—New grains are highlighted in the band contrast map of (a) 550 °C/1 min Base steel and (b) 550 °C/10 min Residual Scrap (RS) steel. The corresponding $\phi_2 = 45$ deg section of ODF of the new grains are given in (c) and (d), respectively.

Texture analyses, Table II, show the new grains in the Base steel exhibit a higher area fraction of γ-fiber than those in the RS steel. Additionally, in both steels, new grains of random orientations formed with a disproportionately high area fraction. For example, in the RS steel, the fraction of random orientation was only 0.104 in the deformed structures; however, it increased to 0.392 in the new recrystallized grains. The random orientations contributed to the background of the ODFs.

Table II. Texture Component Fractions in the New Grains from the 550 °C /1 min Base Steel and 550 °C /10 min Residual Scrap (RS) Steel, Respectively

	Base Steel	RS Steel
α-fiber	0.219	0.232
γ-fiber	0.322	0.256
{411} ⟨148⟩	0.108	0.120
random	0.351	0.392

E. *3.5 TEM Observation*

TEM samples were prepared for the deformed and 650 °C/30 minutes annealed RS steel. Figure 14(a) shows the deformed microstructure characterized by elongated grains with dislocation networks. The EDS maps in Figure 14 reveal the presence of secondary MnS particles of about 20 nm in size, which are expected to form during the reheating and hot rolling stages. TEM investigations on various locations of the FIB specimen did not detect any sign of Cu or Ni precipitates. The overall view of the specimen in Figure 15(a) shows a recrystallized structure with equiaxed grains. Several particles of 200 nm in diameter appear. EDS elemental maps, Figures 15(b2) through (b5), reveal those particles are carbides rich in Cr and Mn, which could be formed during the annealing experiments. Fine MnS particles are also present. Cu or Ni precipitates were not detected. Note that calculations from FactStage indicate that the 0.15 wt pct Cu and 0.16 wt pct Ni content in the Scrap steel are soluble in the Fe matrix above 550 °C in the equilibrium condition. Figures 15c2 and c3 show line profiles for Cu and Mn, respectively, across a grain
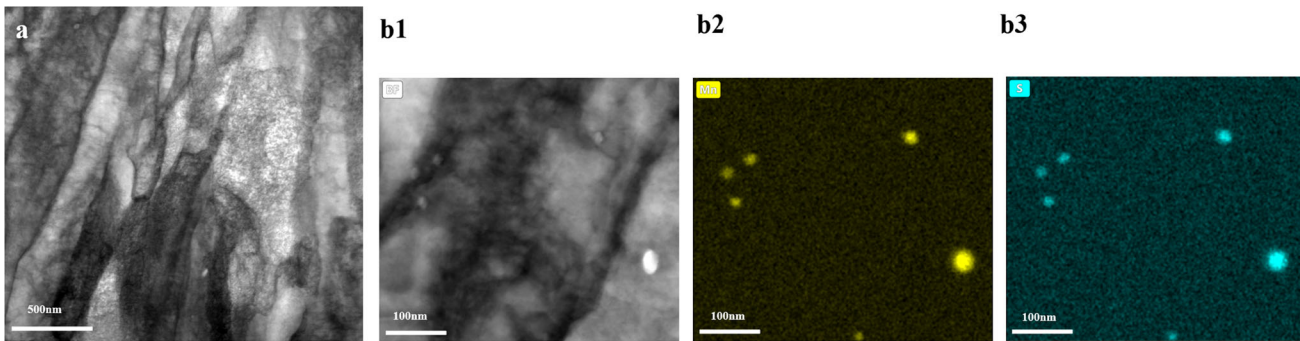

Fig. 14—(*a*) STEM image of the Residual Scrap (RS) steel showing the deformation microstructure; STEM image (*b1*) and EDS chemical maps of Mn (*b2*) and S (*b3*) in the deformed RS steel.
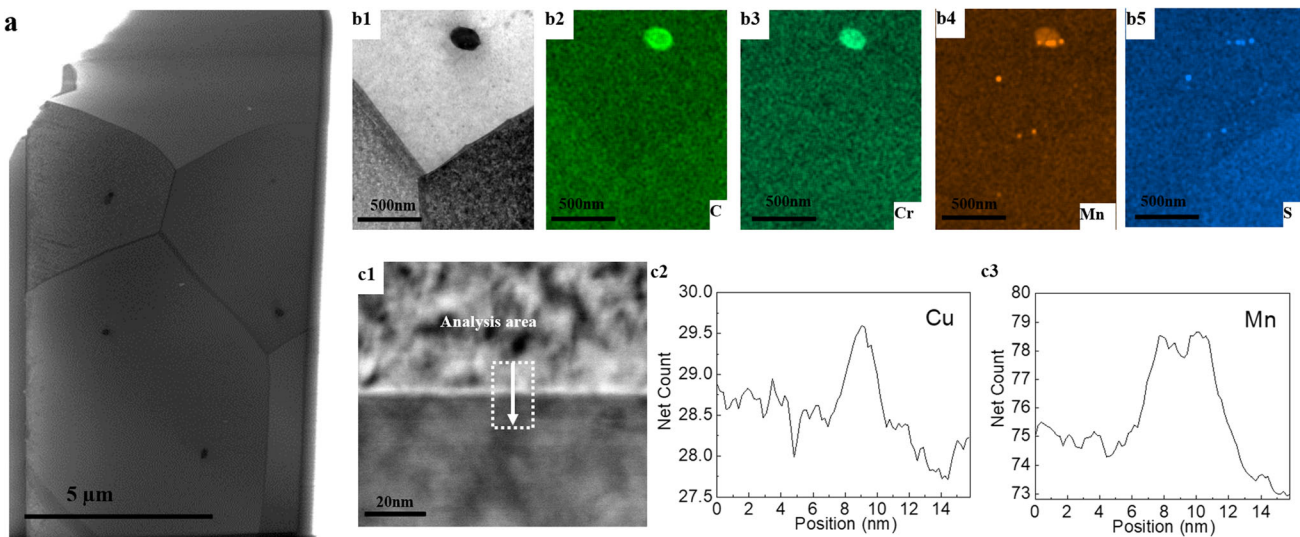

Fig. 15—(*a*) Panoramic STEM image of the 650 °C/30 min Residual Scrap (RS) steel; STEM image (*b1*) and EDS chemical maps of C (*b2*), Cr (*b3*), Mn (*b4*), and S (*b5*) in the annealed RS steel. Line profiles of Cu (*c2*) and Mn (*c3*) across a grain boundary in (*c1*).

boundary from Figure 15(c1). Segregation of Cu and Mn along grain boundaries are observed in the 650 °C/30 minutes annealed Scrap steel. Note that Cu signals were also generated from the TEM sample holder, contributing to the background counts in the Cu map, but a clear peak can be seen at the grain boundary.

Segregation energy for various solute elements at one type of grain boundary, *i.e.*, Σ 5, in bcc Fe has been calculated using Density-functional theory.[34] It was shown that the segregation energy sequence for the relevant solutes is Cu > Ni > Mn > Cr. The observed Cu segregation in Figure 15(c1) can be explained by its high segregation energy, while the Mn segregation could be associated with its considerable bulk concentration. The segregation energy of Sn to GB in bcc Fe has been reported to be 0.52 eV (8.3×10^{-20} J),[35] which is higher than that of Cu. Sn tends to segregate to grain boundaries (as well as to surfaces), and the magnitude of segregation is a function of Sn content, temperature, time, and composition.[36] It is possible that, in the current case, the segregation was too low to be detected by EDS due to its low bulk concentration.

IV. DISCUSSION

Analyses of cold-rolled microstructures and orientations have ascertained that there is a strong correlation between the deformation structures and their orientations. Along the α-fiber, higher misorientation values (Figure 3) and a finer substructure (Figure 2) are associated with higher Φ values. Meanwhile, the γ-fiber overall exhibits higher misorientations and a finer substructure than the α-fiber (Figures 2 through 4). The microstructural heterogeneity indicates the distribution of the stored energy is orientation dependent, which has important implications for recrystallization and texture development.

A. *Microstructure Heterogeneity on Texture Evolution*

Recrystallization consists of the nucleation of new strain-free grains (the so-called 'nucleus') and the growth of those grains. The nucleation is essentially a recovery process when subgrains undergo growth, driven by the energy stored in dislocations and LABs. The new grains need to have HABs so that they have the necessary mobility to grow into the adjacent deformed material. When a region exhibits large orientation gradients, a new grain with HABs will form more rapidly.[37] Next, new grains start to consume the deformed structures. The velocity of the HABs of the grains can be expressed as $V = MP$, where M is the boundary mobility and P is the driving force present from the dislocations and GBs in the adjacent microstructure. Here, P depends on the density and characters of the GBs. The GB energy increases with the increasing misorientation with a cut-off angle of deg15.[27]

Since γ-fiber orientated grains possessed higher stored energy than α-fiber grains, new γ-fiber recrystallized grains could nucleate more quickly and start their growth earlier. Therefore, it is not surprising to see in the recrystallized grains, γ-fiber exhibited a higher fraction than α-fiber, which agrees with the trend observed in other ferritic steels.[21] It is also important to note that the stored energy along the α-fiber is not homogeneously distributed, leading to inhomogeneous weakening of the α-fiber in the recrystallized grains (Figure 12). Here, it is not necessary to involve the selective growth theory to account for the development of γ-fiber. Firstly, EBSD results did not show a significant number of ⟨110⟩ 26.5 deg boundaries in the partial recrystallized structure. Secondly, the results showed that orientations of the early new grains primarily determine the recrystallization textures.

One interesting observation is that random orientations show the greatest fraction increase in the new gains in both steels during recrystallization. A tentative explanation is given as follows. As aforementioned, the random orientations contain high density of LABs, implying they exhibit high stored energy for nucleation. Moreover, they show a HAB density higher than any other textures. HABs are preferred nucleation sites because they give rise to local misorientations due to the operation of different slip systems during deformation.[37] Hence, high HAB density is conducive for the random orientations to nucleate. In addition, the high HABs density in the random orientations can provide large driving force for grain growth.

However, the growth of the random orientation grains was not unconstrained. For example, in both steels annealed at 550 °C, the random orientations occupied higher fractions in the newly recrystallized grains than in the 60 minutes of annealed structure. By checking the partially recrystallized microstructures one can frequently find that the new grains of random orientations clustered together. One example is given in Figure 16. As the nucleation of random orientations could occur more quickly and frequently, the growing grains of random orientations were more likely to meet other random orientation grains from the local regions. Resultantly, those grains were pinned, and further growth became difficult.

During the growth of the new grains, regions of high stored energy were firstly consumed.[38] In the current case, it is not surprising that the α-fiber grains of low stored energy would be retained until the later stage of recrystallization. For the 550 °C/60 minutes RS steel with a recrystallization fraction of ~ 0.8, the corresponding ODF shows that the intensity maximum was at {100} ⟨110⟩. In the intermediate stage of recrystallization, regions oriented in {100} ⟨110⟩ provided limited stored energy and discouraged new grains from invading those regions. While in the recrystallized regions, the textures were weakened by the nucleation and growth of the random orientation grains. The net effect is that the high intensities appear at {100} ⟨110⟩ component from the α-fiber.
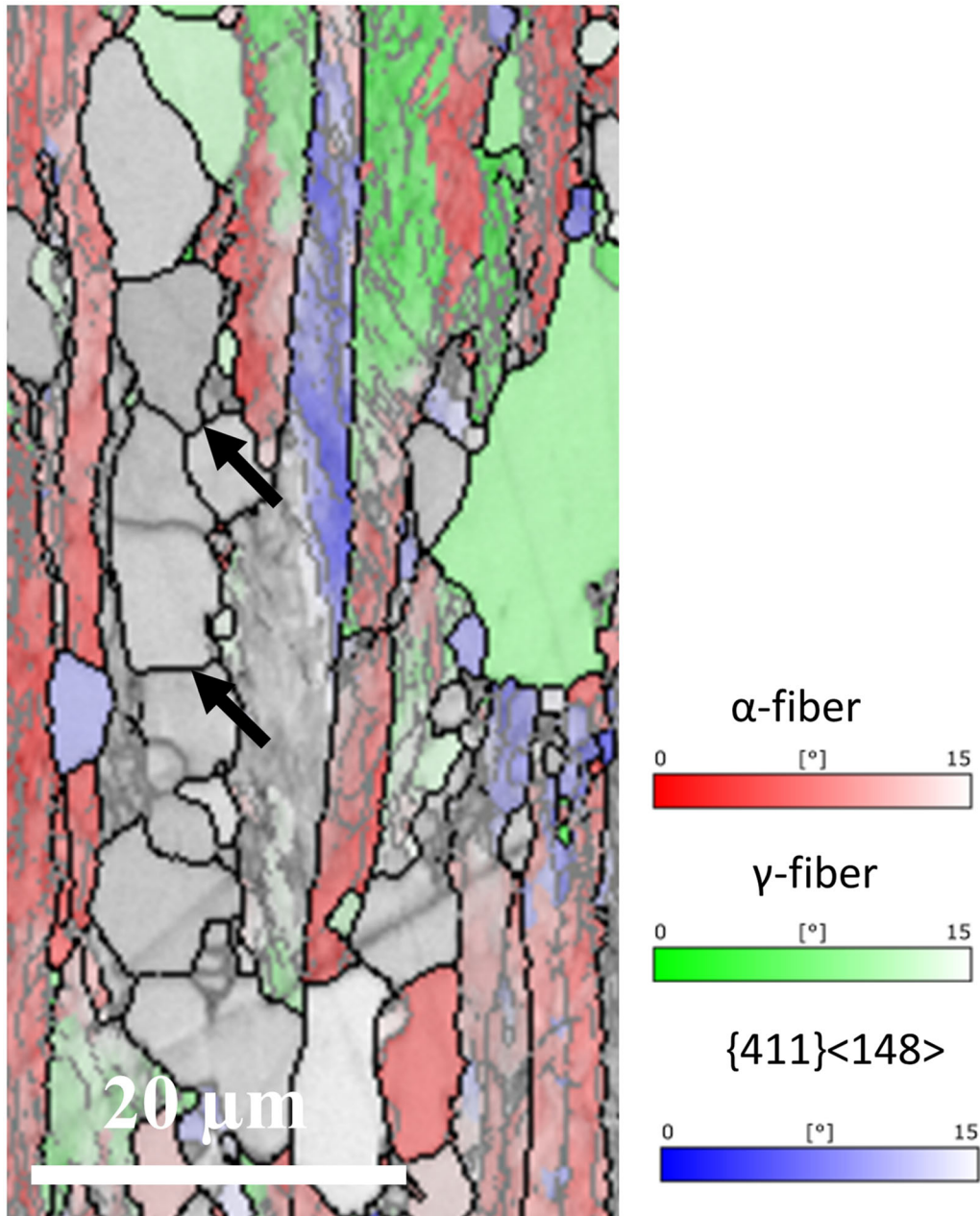
Fig. 16—Partially recrystallized microstructure in the 550 °C/20 min annealed Residual Scrap (RS) steel. The gray regions are of random orientations. Black arrows indicate the pinning of the new grains of random orientations.

B. *Effect of Impurity Elements*

The comparisons in texture evolutions between the Base and RS steels demonstrated that the presence of the impurities has an impact on the annealing textures. RS steel showed lower γ-fiber fractions compared to the Base steel counterpart, and the decrease in γ-fiber fraction was more significant at 550 °C than at higher temperatures. As mentioned, the orientated nucleation was the main mechanism that determined the recrystallization textures; therefore, the effect of solutes on the nucleation of new grains is discussed. Nucleation occurs by subgrain growth to produce new grains with HABs. The subgrain growth depends on the movements of LABs, which are controlled by the climb of dislocations with the help of vacancies.[39,40] It was proposed that when solute atoms are present, they tend to segregate around the dislocations, and the interactions between the solute atoms and dislocations slow down the dislocation velocity, as the vacancies need to escape from the solute atoms first before they migrate to dislocations to initiate the subgrain boundary movement.[40] The presence of alloying elements gives rise to the activation energy for the diffusion of Fe atoms, and the process requires the vacancies to overcome the solute-vacancy binding energy, $E_{\rm b}^{\rm solute-vac}$. Faulknerv et al.[41] proposed a model for calculating $E_{\rm b}^{\rm solute-vac}$ in

Table III. Parameters for the Effect of Impurities on the Dislocation Velocity in Eqs. [1] through [4]

Symbol	Cu	Ni	Cr	Sn
X_{solute}(wt pct)	0.15	0.16	0.12	0.04
$r_{\text{solute}}(10^{-12}m)$	138	121	127	141
$E_{\text{b}}^{\text{solute-dis}}(10^{-20}J)$	6.09	1.87	0.94	7.50
$E_{\text{b}}^{\text{solute-vac}}* (10^{-20}J)$	7.18	2.05	1.03	7.70

Values of the * marked parameter are obtained from Ref. [41]

steels. The average escape energy, E^{esc}, is proportional to the solute segregation level at dislocations, $X_{\text{dis}}^{\text{solute}}$:

$$E^{\text{esc}} = X_{\text{dis}}^{\text{solute}} \cdot E_{\text{b}}^{\text{solute-vac}}. \qquad [1]$$

The $X_{\text{dis}}^{\text{solute}}$ in equilibrium is expressed as[42]

$$X_{\text{dis}}^{\text{solute}} = \frac{X_{\text{solute}} \exp\left(\frac{E_{\text{b}}^{\text{solute-dis}}}{kT}\right)}{1 + X_{\text{solute}} \exp\left(\frac{E_{\text{b}}^{\text{solute-dis}}}{kT}\right)}, \qquad [2]$$

where X_{solute} is the bulk concentration of the solute, $E_{\text{b}}^{\text{solute-dis}}$ is the binding energy between the solutes and the dislocations, $k = 1.38 \times 10^{-23} J \cdot K^{-1}$ is Boltzmann's constant, and T is the temperature. The $E_{\text{b}}^{\text{solute-dis}}$ is estimated as[43]

$$E_{\text{b}}^{\text{solute-dis}} = 4G \cdot r_{\text{Fe}}^3 \cdot \left| \frac{r_{\text{Fe}} - r_{\text{solute}}}{r_{\text{Fe}}} \right|, \qquad [3]$$

where $r_{\text{Fe}} = 1.25 \times 10^{-10}$ m is the atomic radius of Fe, and r_{solute} is the atomic radius the solute, and $G = 75$ GPa is the shear modulus. The relative velocity of the dislocations with solutes (v) with respect to those in pure iron (v_0) can be expressed as[40]

$$\frac{v}{v_0} = \exp\left(\frac{-E^{\text{esc}}}{kT}\right). \qquad [4]$$

Based on Eqs. [1] through [4], the magnitude of retardation of a certain kind of solute at given temperatures is associated with the bulk concentration of the solute and the size mismatch between the solute and the Fe atoms. A higher concentration and a higher size mismatch give rise to a higher E^{esc}, thus the dislocation velocity and subgrain boundary migration will be more suppressed.

All the solutes present in the low-carbon steel can exert some degree of dragging force to the dislocations. To understand how the impurities affect the dislocation velocity (hence the retardation of nucleation), the V/V_0 was calculated for the cases when each species of solute exists as well as the case in the RS steel when all the impurities are present. The input parameters for the calculation using Eqs. [1] through [4] are listed in Table III, and V/V_0 values against the temperature are plotted in Figure 17. Note that, in addition to Cu and Ni mentioned in Sect. 3.5, 0.12 wt pct Cr and 0.04 pct Sn should also be soluble in Fe in equilibrium at the temperatures of interests, based on FactStage
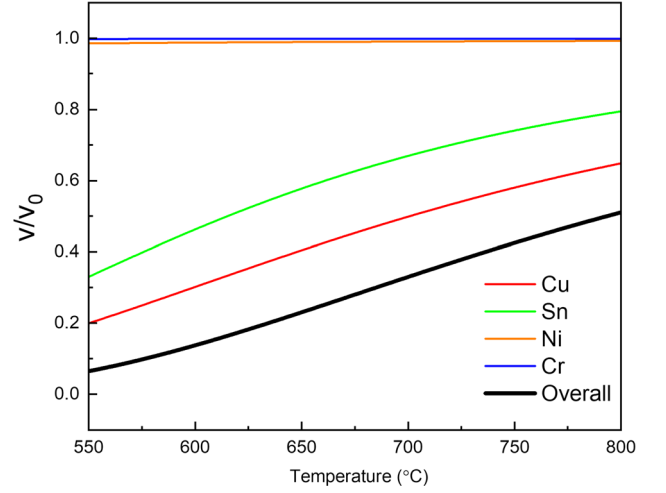

Fig. 17—The relative velocity of the dislocations with solutes with respect to those in pure iron (V/V_0). The effects of the individual specie of solute as well as their overall effects are considered.

calculation. The overall effect of the impurities was considered by summing up the E^{esc} of each kind of solute as the overall E^{esc}. The calculations indicate that Cu has the greatest retarding effect on the dislocation velocity, followed by Sn, while the effect of Ni and Cr appear to be negligible. Meanwhile, the V/V_0 value increases with increasing temperature regardless of the solutes type, indicating the effect of solute atoms on the dislocation velocity becomes weakened at higher temperatures.

When the impurity atoms suppressed the dislocation velocity in the RS steel, the γ-fiber nucleation was retarded, especially at low temperatures, delaying the time for subsequent growth. On the other hand, the development of random orientations nucleation depended more on the high density of HABs that provides large driving force for grain growth. After nucleation, grains of random orientations can quickly grow into the deformed structures. Therefore, a higher fraction of random orientations can be developed in the RS steel. At higher temperatures (> 650 °C), the suppression of the dislocation movement was reduced (Figure 17), hence a higher fraction of γ-fiber can be obtained. However, the effect of the impurities was persistent. Comparing to the Base steel, the fraction of γ-fiber was lower and that of the random orientations was higher in the RS steel for each annealing condition.

V. CONCLUSION

Impurities were added to a low-carbon formable steel to simulate the scenario of increased used of scrap during steel production. The effect of the impurities on the microstructure and texture evolution in the steel was studied, and the conclusions are as follows:

1. In the cold-rolled condition, both the Base steel and the RS steel showed typical thin-banded grains and exhibited well-developed α-fiber, γ-fiber and {411}

⟨148⟩ textures. The addition of impurities did not produce visible difference in the cold-rolled microstructure nor in the overall textures.

2. It was ascertained that the deformation microstructures were orientation dependent in the low-carbon steel. KAM calculations indicated that the γ-fiber grains showed higher intragranular misorientations than the α-fiber grains. Along the α-fiber, misorientations increased with increasing Φ. The analyses of the areal density of the (sub)grain boundaries showed that γ-fiber grains also contained a higher areal LAB and HAB density than the α-fiber grains. Random orientation grains were found to contain the highest areal HAB density.

3. Impurities were shown to be detrimental to the development of γ-fiber texture during annealing. It is proposed that the impurity solutes, such as Cu and Sn, retarded the dislocation movement, hence the nucleation of γ-fiber was suppressed. At higher temperatures, the adverse effect caused by the impurity solutes was less.

4. Random orientations increased their fraction during recrystallization. It was proposed that the high areal HAB density measured in the random orientation regions facilitated the nucleation and growth of the random orientation grains.

CONFLICT OF INTEREST

The authors declare that they have no conflict of interest.

REFERENCES

1. S. Spooner, C. Davis, and Z. Li: *Ironmak. Steelmak.*, 2020, vol. 47, pp. 1100–113.
2. C. Wang, M. Brämming, and M. Larsson: *Steel Res. Int.*, 2013, vol. 84, pp. 387–94.
3. EU-27 Steel Scrap Specification European Ferrous Recovery and Recycling Federation, (Brussels, Belgium 2007).
4. J. Duan, D. Farrugia, C. Davis and Z. Li, *Ironmak. Steelmak.* 2021, pp. 1–7.
5. U.F. Kocks, C.N. Tomé and H.-R. Wenk: *Texture and anisotropy: preferred orientations in polycrystals and their effect on materials properties* (Cambridge University Press, 1998).
6. R.K. Ray: JJ Jonas and RE Hook. *Int. Mater. Rev.*, 1994, vol. 39, pp. 129–72.
7. M.Y. Huh and O. Engler: *Mater. Sci. Eng. A*, 2001, vol. 308, pp. 74–87.
8. D. Raabe, Y. Wang, and F. Roters: *Comput. Mater. Sci.*, 2005, vol. 34, pp. 221–34.
9. P. Ghosh, C. Ghosh, R.K. Ray, and D. Bhattacharjee: *Scripta Mater.*, 2008, vol. 59, pp. 276–78.
10. J.-I. Hamada, N. Ono, and H. Inoue: *ISIJ Int.*, 2011, vol. 51, pp. 1740–748.
11. Y. Z. Li, S. L. Zhao, S. H. He, C. P. Huang and M. X. Huang, *Int. J. Plast.* 2022, vol. 155.
12. H. Inagaki: *ISIJ Int.*, 1994, vol. 34, pp. 313–21.
13. P.S. Bate, J. Quinta, and da Fonseca: *Mater. Sci. Eng. A*, 2004, vol. 380, pp. 365–77.
14. P. Van Houtte, S. Li, M. Seefeldt, and L. Delannay: *Int. J. Plast*, 2005, vol. 21, pp. 589–624.
15. A. Molinari, G.R. Canova, and S. Ahzi: *Acta Metall.*, 1987, vol. 35, pp. 2983–94.
16. A. Després, M. Zecevic, R.A. Lebensohn, J.D. Mithieux, F. Chassagne, and C.W. Sinclair: *Acta Mater.*, 2020, vol. 182, pp. 184–96.
17. B. Hutchinson: *Philos. Trans. R. Soc. Lond. Ser. A*, 1999, vol. 357, pp. 1471–85.
18. D.P. Field, C.C. Merriman, N. Allain-Bonasso, and F. Wagner: *Modell. Simul. Mater. Sci. Eng.*, 2012, vol. 20, 024007.
19. L.A.I. Kestens and H. Pirgazi: *Mater. Sci. Technol.*, 2016, vol. 32, pp. 1303–15.
20. N. Rajmohan, Y. Hayakawa, J.A. Szpunar, and J.H. Root: *Acta Mater.*, 1997, vol. 45, pp. 2485–94.

21. D. Hawezy and S. Birosca: *Acta Mater.*, 2021, vol. 216, 117141.
22. M.Z. Quadir and B.J. Duggan: *Acta Mater.*, 2004, vol. 52, pp. 4011–21.
23. A. Ayad, M. Ramoul, A.D. Rollett, and F. Wagner: *Mater. Charact.*, 2021, vol. 171, 110773.
24. M.Z. Quadir and B.J. Duggan: *Acta Mater.*, 2006, vol. 54, pp. 4337–50.
25. A.A. Gazder: M. Sánchez-Araiza, J.J. Jonas and E.V. Pereloma. *Acta Mater.*, 2011, vol. 59, pp. 4847–65.
26. I. Kapoor, Y. Lan, A. Rijkenberg, Z. Li, and V. Janik: *Mater. Charact.*, 2018, vol. 145, pp. 686–96.
27. F.J. Humphreys: *Acta Mater.*, 1997, vol. 45, pp. 4231–40.
28. K. Verbeken, L. Kestens, and J.J. Jonas: *Scripta Mater.*, 2003, vol. 48, pp. 1457–62.
29. K. Ushioda, N. Yoshinaga, and O. Akisue: *ISIJ Int.*, 1994, vol. 34, pp. 85–91.
30. F. Emren, U. von Schlippenbach, and K. Lücke: *Acta Metall.*, 1986, vol. 34, pp. 2105–17.
31. R. Barbosa, F. Boratto, S. Yue and J.J. Jonas, *Process. Microstruct. Proper. HSLA Steels* 1987, pp. 51–61.
32. B.L. Li, A. Godfrey, Q.C. Meng, Q. Liu, and N. Hansen: *Acta Mater.*, 2004, vol. 52, pp. 1069–81.
33. H. Homma, S. Nakamura, and N. Yoshinaga: *Mater. Sci. Forum*, 2004, vol. 467–470, pp. 269–74.
34. H. Jin, I. Elfimov, and M. Militzer: *J. Appl. Phys.*, 2014, vol. 115, 093506.
35. S. Suzuki, K. Kuroki, H. Kobayashi, and N. Takahashi: *Mater. Trans. JIM*, 1992, vol. 33, pp. 1068–76.
36. H.J. Grabke: *ISIJ Int.*, 1989, vol. 29, pp. 529–38.
37. J. Humphreys, G.S. Rohrer and A. Rollett, In *Recrystallisation and related annealing phenomena (Third Edition)*, ed. J. Humphreys, G.S. Rohrer, and R. Anthony (Elsevier: Oxford, 2017), pp 245–304.
38. J. Duan, H. Wen, C. Zhou, X. He, R. Islamgaliev and R. Valiev, *Mater. Charact.* 2020, vol. 159.
39. D.G. Cram, X.Y. Fang, H.S. Zurob, Y.J.M. Bréchet, and C.R. Hutchinson: *Acta Mater.*, 2012, vol. 60, pp. 6390–6404.
40. M. Winning, A.D. Rollett, G. Gottstein, D.J. Srolovitz, A. Lim, and L.S. Shvindlerman: *Phil. Mag.*, 2010, vol. 90, pp. 3107–128.
41. R.G. Faulkner, S.H. Song, and P.E.J. Flewitt: *Mater. Sci. Technol.*, 1996, vol. 12, pp. 904–10.
42. N. Louat: *Philos. Mag. A*, 1981, vol. 44, pp. 223–28.
43. Alan Howard Cottrell: *Am. J. Phys.*, 1954, vol. 22, pp. 242–43.